

# Filamentation-assisted self-compression of subpetawatt laser pulses to relativistic-intensity subcycle field waveforms

P. A. Zhokhov,<sup>1</sup> V. Ya. Panchenko,<sup>2,3</sup> and A. M. Zheltikov<sup>1,3,4</sup>

<sup>1</sup>*Department of Physics and Astronomy, Texas A & M University, College Station, TX 77843, USA*

<sup>2</sup>*Institute of Laser and Information Technologies, Russian Academy of Sciences, ul. Svyatoozerskaya 1, Shatura, Moscow Region 140700, Russia*

<sup>3</sup>*Kurchatov Institute Russian Research Center, pl. akad. Kurchatova 1, Moscow 123098, Russia*

<sup>4</sup>*Physics Department, Russian Quantum Center, International Laser Center, M.V. Lomonosov Moscow State University, Moscow 119992, Russia*

(Received 6 March 2012; published 23 July 2012)

Filamentation-assisted spatiotemporal dynamics of ultrashort laser pulses in the regime of extreme light powers is shown to enable self-compression of subpetawatt laser pulses to relativistic field intensities and subcycle pulse widths. Our supercomputer simulations demonstrate compression of 6-J, 30-fs laser pulses at a central wavelength of 800 nm to 1.3-fs sub-100-TW broadband field waveforms and reveal the generation of relativistic-intensity subfemtosecond field transients as a result of such a pulse evolution scenario, with multiple filamentation avoided due to low gas pressures and the balance between Kerr and ionization nonlinearities steered toward optimal pulse compression due to the depletion of outer-shell ionization in a high-intensity laser field.

DOI: [10.1103/PhysRevA.86.013835](https://doi.org/10.1103/PhysRevA.86.013835)

PACS number(s): 42.65.Re

## I. INTRODUCTION

Filamentation of ultrashort laser pulses is one of the key effects in high-field ultrafast optical science [1–3]. The physics behind this interesting and practically significant phenomenon involves a complex, strongly coupled spatiotemporal dynamics of optical field waveforms, which gives rise to a unique regime of short-pulse propagation, where the self-focusing of an intense laser beam induced by the Kerr optical nonlinearity is counterbalanced by plasma refraction [2,3]. Laser-induced filamentation offers promising solutions for the long-range transmission of high-power electromagnetic radiation [4], spectral superbroadening of high-power ultrashort laser pulses [2,3], terahertz radiation generation [5], and the remote sensing of the atmosphere [6]. In ultrafast optical science, this phenomenon finds growing applications as a powerful technique for pulse compression [7,8], enabling the generation of high-peak-power carrier-envelope-phase stable few-cycle optical field waveforms within a broad frequency range from the deep ultraviolet [9,10] to the near- and mid-infrared [11].

Development of extreme-power advanced laser sources [12] calls for an upscaling of filamentation-based strategies of pulse compression to higher peak powers. Such an extension, however, encounters fundamental physical difficulties related to the instability of high-power laser beams with respect to small intensity variations across the laser beam and small spatial inhomogeneities in the optical properties of nonlinear media [13], giving rise to a multifilamentary structure of the laser beams at high levels of peak powers [2,3].

Here, we show that filamentation-assisted compression of subpetawatt laser pulses is possible in low-pressure gases, where the gas pressure is chosen in such a way as to avoid multiple filamentation and where the depletion of outer-shell ionization is used to steer the balance between Kerr nonlinearity-induced self-focusing and plasma defocusing toward the optimum for self-compression of subpetawatt laser pulses.

## II. MODEL

To model the spatiotemporal dynamics of extreme-power laser pulses in a nonlinear, fast-ionizing gas, we numerically solve, in parallel codes, the generalized nonlinear Schrödinger equation (GNSE) [2,3], modified to include effects related to the multiple ionization of the gas as described below. The formation of a robust, cylindrically symmetric single filament was verified by numerically solving the full (3 + 1)-dimensional GNSE:

$$\frac{\partial A(\omega)}{\partial z} = i \left( D(\omega) + \frac{i \nabla_{\perp}^2}{2k(\omega)} \right) A(\omega) + R_{\text{NL}} + R_{\text{pl}}, \quad (1)$$

where  $A \equiv A(t, r, z)$  is the complex field envelope,  $t$  is the retarded time,  $z$  is the coordinate along the propagation axis,  $\mathcal{F}_{t \rightarrow \omega}[\dots]$  denotes time-to-frequency Fourier transform,  $A(\omega) \equiv \mathcal{F}_{t \rightarrow \omega}[A]$  is the field spectrum,  $D(\omega) = (k(\omega) - \frac{\omega}{V_{\text{gr}}})$  is the dispersion operator,  $k(\omega) = n(\omega) \frac{\omega}{c}$  is the wave number,  $n(\omega)$  is the frequency-dependent field-free refractive index,  $V_{\text{gr}}$  stands for the group velocity at the central frequency  $\omega_0$  of the pulse,  $\nabla_{\perp}^2 = \frac{\partial^2}{\partial x^2} + \frac{\partial^2}{\partial y^2}$  is the transverse part of the Laplace operator,  $x$  and  $y$  are the two transverse coordinates,  $R_{\text{NL}}$  is the nonlinear response of bound electrons, including the Kerr-type nonlinearity, and  $R_{\text{pl}}$  is the nonlinear response of free electrons produced by the high-power laser field.

Following this step, the details of the spatiotemporal dynamics of the laser pulse were analyzed for the cylindrically symmetric case using the (2 + 1)-dimensional GNSE, written in the form of Eq. (1) with  $\nabla_{\perp}^2 = \frac{1}{r} \frac{\partial}{\partial r} (r \frac{\partial}{\partial r})$ , where  $r$  is the radial coordinate.

The nonlinear response of bound electrons  $R_{\text{NL}}$  is defined as

$$R_{\text{NL}} = i \frac{\omega}{c} \mathcal{F}_{t \rightarrow \omega} \left[ n_2 \left( |A|^2 A + \frac{1}{3} A^3 \right) \right] + i \frac{\omega}{c} \mathcal{F}_{t \rightarrow \omega} \left[ n_4 \left( |A|^4 A + \frac{1}{2} |A|^2 A^3 \right) \right], \quad (2)$$

where  $n_2$  and  $n_4$  are the Kerr nonlinear refractive indices. The  $|A|^2 A$  and  $|A|^4 A$  terms describe intensity-dependent refraction, while the  $\frac{1}{3}A^3$  and  $\frac{1}{2}|A|^2 A^3$  terms account for third-harmonic generation through the third- and fifth-order nonlinear susceptibilities.

The  $R_{\text{pl}}$  function on the right-hand side of Eq. (1) includes ionization effects,

$$R_{\text{pl}} = -\frac{\sigma(\omega)}{2}(1 + i\omega\tau_c)\mathcal{F}_{t \rightarrow \omega}[\rho(t)A] - \mathcal{F}_{t \rightarrow \omega}\left[\sum_{Z=0}^N \frac{U_Z + U_p}{|A|^2} W_Z A\right], \quad (3)$$

where  $\sigma(\omega) = \frac{\mu_0 e^2}{mk(\omega)(1+\omega^2\tau_c^2)}$  is the inverse bremsstrahlung cross section,  $\mu_0$  is vacuum permeability,  $e$  and  $m$  stand for the electron charge and mass, respectively, and  $\tau_c$  is the electron momentum transfer time. The last term on the right-hand side of Eq. (3) accounts for the photoionization losses,  $U_Z$  and  $W_Z$  are the ionization potential and photoionization rate for an ion with a charge  $Z$ , and  $U_p$  is the electron ponderomotive energy. The time-dependent free electron density  $\rho(t)$  is found by integrating the following set of equations [14]:

$$\frac{\partial \rho_0}{\partial t} = -W_0 \rho_0, \quad (4)$$

$$\frac{\partial \rho_Z}{\partial t} = W_{Z-1} \rho_{Z-1} - W_Z \rho_Z \quad \text{for } Z = 1, \dots, N, \quad (5)$$

$$\rho = \sum_{Z=1}^N Z \rho_Z, \quad (6)$$

where  $\rho_Z$  is the density of ions with a charge  $Z$ , subject to the initial conditions

$$\rho_Z(t=0) = 0 \quad \text{for } Z = 1, \dots, N, \quad (7)$$

$$\rho_0(t=0) = \rho_{\text{at}}, \quad (8)$$

where  $\rho_{\text{at}}$  is the density of neutral atoms.

Simulations were performed for low-pressure argon. Dispersion was included in the model through the appropriate Sellmeier equation for argon [15]. The nonlinear refractive indices are calculated as  $n_{2,4} = \bar{n}_{2,4} \frac{p}{p_0}$ , where  $p$  is the gas pressure and  $p_0$  is the atmospheric pressure. The values of the nonlinear refractive index  $\bar{n}_2$  for argon available from the literature vary within at least the range from  $0.8 \times 10^{-19}$  to  $1.5 \times 10^{-19} \text{ cm}^2 \text{ W}^{-1}$  [16–19]. For our simulations, we take  $\bar{n}_2 = 10^{-19} \text{ cm}^2 \text{ W}^{-1}$ . Since all the Kerr-type processes in our system are controlled by the product of  $\bar{n}_2$  and the gas pressure  $p$ , the uncertainty in  $\bar{n}_2$  simply implies an additional adjustment of the gas pressure  $p$ . The critical power for self-focusing at  $p = 1$  bar for radiation with the wavelength  $\lambda_0 = 800$  nm is then equal to  $P_{\text{cr}} = \frac{3.77\lambda_0^2}{8\pi n_2 n_0} \approx 9.6$  GW. The electron momentum transfer time was calculated as  $\tau_c = \bar{\tau}_c \frac{p_0}{p}$  with  $\bar{\tau}_c = 190$  fs for argon [2,3]. In electron density calculations, it was sufficient to limit the sum in Eqs. (3) and (4) with  $N = 11$ , as the number of  $\text{Ar}^{11+}$  ions was negligibly small. Throughout the paper, we discuss simulations performed for a Gaussian pulse with a FWHM pulse width  $\tau_0 = 30$  fs and the central wavelength  $\lambda_0 = 800$  nm. Light pulses with such parameters and energies in the range of

a few joules can be routinely generated by the available 100–200-TW laser systems [20,21]. Simulations done with other input pulse shapes, including flat-top, super-Gaussian pulses, show that because of the highly nonlinear, strongly coupled temporal and spatial field waveform dynamics, which involves pulse and beam sectioning, it is nontrivial to identify simple pulse-shaping strategies that would efficiently optimize filamentation-assisted pulse compression or enhance its energy throughput in the considered range of field intensities. The input beam diameter and the focusing length were varied in our (3+1)-dimensional simulations in order to achieve the highest efficiency of pulse compression simultaneously avoiding the multiple filamentation of a beam, as discussed below in this paper. In what follows, we present the results of simulations performed for a Gaussian laser beam with an initial FWHM diameter of 2 cm and a linear focal length of 5 m. This beam focusing geometry was found to provide the most promising regime of pulse compression.

### III. COMPUTATION

Numerical integration of Eqs. (1)–(4) was performed using the split-step method. At each step in  $z$ , the variation in the complex amplitude  $A$  due to  $R_{\text{NL}}$  and  $R_{\text{pl}}$  is calculated using the fourth-order Runge-Kutta method. For (3+1)-dimensional GNSE simulations, the grid includes  $1024 \times 4096 \times 4096 = 2^{34}$  points in  $t$ ,  $x$ , and  $y$ , respectively, with a time step  $\Delta t = 0.4$  fs and a spatial step  $\Delta x = \Delta y = 20 \mu\text{m}$ . The integration step  $\Delta z$  was adaptively adjusted to keep the nonlinear phase shift at each step below 0.01 rad. On the average, about  $6 \times 10^3$  steps in  $z$  are needed to simulate the dynamics of a laser pulse within a 7-m propagation path. In (2+1)-dimensional GNSE simulations, an exponential grid in  $r$  was used. Simulations were performed on the Lomonosov Moscow State University supercomputer using 1024 Intel Xeon Nehalem cores for (3+1)-dimensional simulations and 64 cores for (2+1)-dimensional simulations with 75 000 and 400 CPU hours per run, respectively.

### IV. RESULTS AND DISCUSSION

To avoid multiple filamentation of the high-power laser beam, the gas pressure in our analysis is chosen in such a way as to keep the critical power for self-focusing  $P_{\text{cr}}$  approximately at the level of the peak power  $P$  of the laser pulse. In particular, for a 30-fs pulse with  $E_0 = 6$  J, the peak power becomes equal to  $P_{\text{cr}}$  at an argon pressure of  $5.11 \times 10^{-5}$  bar.

As a first step of our analysis, we verify that the high-power laser pulse with a given initial energy forms a single filament as it propagates through the low-pressure gas, with its beam profile remaining stable with respect to the buildup of a small-scale multifilamentary beam structure. Figure 1(a) presents the results of (3+1)-dimensional simulations for a 30-fs laser pulse with an energy of 6 J, propagating in argon at  $p = 5.11 \times 10^{-5}$  bar, with  $P = P_{\text{cr}}$ . The beam at the linear focus point  $z = 0$  displays perfect cylindrical symmetry with no signatures of multiple filamentation.

However, avoiding multiple filamentation by keeping  $P_{\text{cr}} \approx P$  at lower gas pressures is necessary, but not sufficient to effectively scale filamentation-assisted pulse compression to

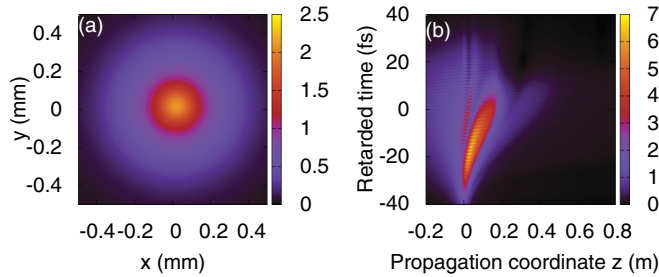


FIG. 1. (Color online) (a) The fluence  $F = \int |A|^2 dt$  ( $\text{kJ}/\text{cm}^2$ ) as a function of transverse coordinates  $x$  and  $y$  of a high-power beam with  $E_0 = 6$  J,  $\tau_0 = 30$  fs, and  $\lambda_0 = 800$  nm at  $z = 0.4$  m in argon at  $p = 5.11 \times 10^{-5}$  bar simulated by solving the (3 + 1)-dimensional GNSE. (b) The on-axis field intensity ( $\text{PW}/\text{cm}^2$ ) as a function of the propagation distance and retarded time for  $E_0 = 1$  J,  $\tau_0 = 30$  fs, and  $P = P_{\text{cr}}$ .

extreme light powers. Since the ionization rate is typically a much steeper function of the laser intensity than the Kerr nonlinearity, efficient pulse compression of extreme-power laser pulses at low gas pressures is prevented [Figs. 1(b) and 2(a)] by a fast increase in the electron density along the filament [dashed curve in Fig. 2(a)], which tends to defocus the laser beam following the initial stage of beam self-focusing [Fig. 1(b)]. To steer the balance between ionization-induced defocusing and Kerr-nonlinearity-related self-focusing toward more efficient pulse compression in longer filaments, we use specific properties of argon, which features a large gap ( $\Delta U \approx 280$  eV) between the ionization potentials of  $M$ - and  $L$ -shell electrons. When the laser field intensity is high enough to deplete the  $M$  shell, the large gap  $\Delta U$  tends to stabilize the electron density along the filament. This effect is illustrated by Fig. 2(a), showing that 1- and 6-J laser pulses generate filaments where the maximum field intensities differ by two orders of magnitude, while the average ionization degrees  $\langle Z \rangle = \rho/\rho_{\text{at}}$  differ only by factor of 2. This result is in striking contrast with filamentation at the atmospheric pressure, when the electron density rapidly grows with the laser intensity [2,3]. For  $E_0 = 6$  J, the average ionization degree  $\langle Z \rangle$  is effectively clamped at  $\langle Z \rangle = 8$  (which corresponds to

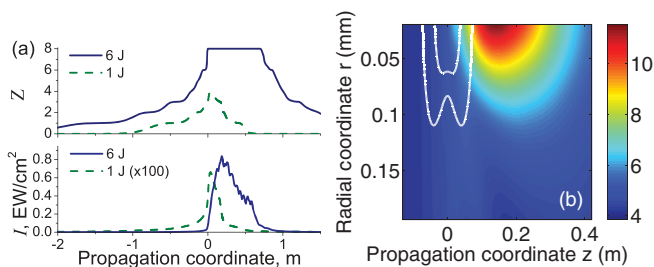


FIG. 2. (Color online) (a) The ionization degree (top) and the maximum on-axis field intensity (bottom) vs the propagation coordinate  $z$  for  $\tau_0 = 30$  fs,  $P = P_{\text{cr}}$ , and  $E_0 = 1$  J (dashed lines) and 6 J (solid lines). (b) The fluence ( $\text{kJ}/\text{cm}^2$ ) as a function of the propagation distance  $z$  and radial coordinate  $r$  for  $E_0 = 6$  J,  $\tau_0 = 30$  fs,  $P = P_{\text{cr}}$ . The levels of 0.1 and 0.3 of the maximum field intensity for a linearly focused beam are shown by white contour lines.

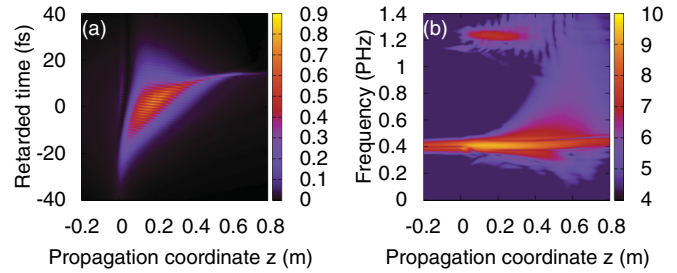


FIG. 3. (Color online) (a) The on-axis field intensity ( $\text{EW}/\text{cm}^2$ ) as a function of the propagation distance and retarded time and (b) the on-axis spectral intensity in arbitrary units on the log scale as a function of the propagation distance and frequency for  $E_0 = 6$  J,  $\tau_0 = 30$  fs, and  $P = P_{\text{cr}}$ .

a complete depletion of the  $M$  shell) and remains unchanged over more than 1 m.

Due to this electron density clamping effect, the Kerr-nonlinearity-related phenomena can be decoupled within a limited time interval and limited propagation path from ionization-induced defocusing, as the laser intensity can increase [Fig. 2(a)] without a noticeable growth in the electron density [solid curve, the range of intensities from 0.2 to 0.8  $\text{EW}/\text{cm}^2$  in Fig. 2(a)]. The spatial self-action of a high-power laser beam under these conditions is dominated by the Kerr nonlinearity, enabling efficient pulse compression through pulse self-steepening and space-time focusing [2,3].

This regime of pulse self-compression is illustrated in Figs. 3(a) and 3(b), which present the spatiotemporal dynamics and dynamics of spectral broadening of a laser pulse with  $\tau_0 = 30$  fs and energy 6 J in argon at  $p = 5.11 \times 10^{-5}$  bar with  $\bar{n}_4 = 0$ . Behind the linear focus [ $z = 0$ , shown by white contour lines in Fig. 2(b)], the beam continues to focus due to the Kerr nonlinearity [Fig. 2(b)], which dominates within this section of propagation path over ionization-induced defocusing, suppressed due to the depletion of ionization from the outer shell of argon. This beam self-focusing dynamics is accompanied by pulse reshaping and compression in the time domain, as well as by efficient supercontinuum generation in the spectral domain. At  $z = 0.5$  m, the spectrum of this supercontinuum stretches into the UV region, where it starts to interfere with the third harmonic (the spectral component centered at 1.2 PHz).

Maximum pulse compression is achieved at a certain distance inside a filament ( $z = 0.6$  m for the chosen set of parameters, see Figs. 4 and 5). This distance of maximum compression depends on the gas pressure. As the pressure of argon is increased from  $5.11 \times 10^{-5}$  bar (the pressure that provides compression to the shortest pulse width) to  $6 \times 10^{-5}$  bar, maximum compression to a pulse width of about 3 fs is achieved at  $z = 0.5$  m.

In Fig. 4(a), we show the FWHM pulse width, the rms pulse width

$$\tau_{\text{rms}} = \sqrt{\frac{\int_0^{r_0} r dr \int dt |A|^2 t^2}{\int_0^{r_0} r dr \int dt |A|^2} - \left( \frac{\int_0^{r_0} r dr \int dt |A|^2 t}{\int_0^{r_0} r dr \int dt |A|^2} \right)^2},$$

where  $r_0$  is the aperture of, e.g., a pinhole used to select the central part of the beam at  $z = 0.6$  m. With  $r_0 = 0.14$  mm,

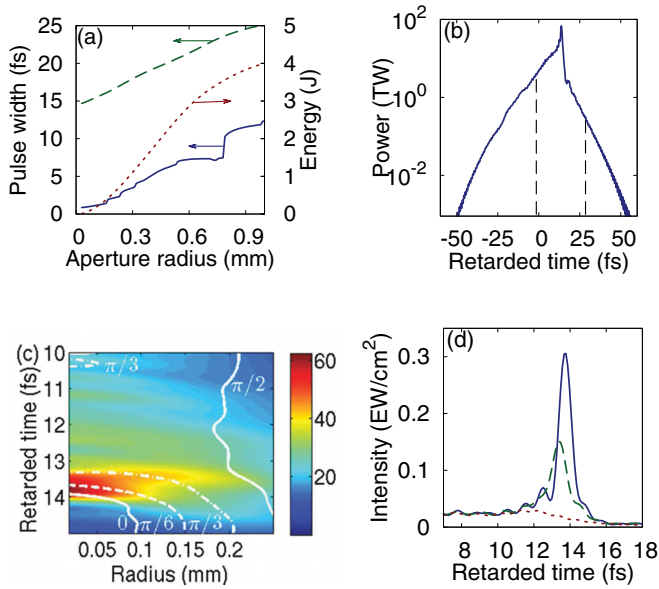


FIG. 4. (Color online) (a) The FWHM pulse width (solid blue line), the rms pulse width (dashed green line), and the total energy (red dotted line) for the compressed pulse transmitted through an aperture with a radius  $r_0$  at  $z = 0.6$  m, (b) the power in the pulse (log scale) transmitted through an aperture with a radius of 0.14 mm at  $z = 0.6$  m. The vertical dashed lines show the initial pulse width. (c) The maps of the field intensity (PW/cm<sup>2</sup>) vs retarded time and radius at  $z = 0.65$  m. White contour lines are the isolines of the temporal phase. (d) The on-axis field intensity vs the retarded time at  $z = 0.6$  m for  $\bar{n}_4 = 0$  (blue solid line),  $-1 \times 10^{-39}$  cm<sup>4</sup>/W<sup>2</sup> (green dashed line),  $-1 \times 10^{-38}$  cm<sup>4</sup>/W<sup>2</sup> (red dotted line). In all cases  $E_0 = 6$  J,  $\tau_0 = 30$  fs, and  $P = P_{cr}$ .

pulses with an FWHM pulse width of 1.3 fs and a total energy of about 0.3 J can be generated [Fig. 4(b)]. The contrast of this pulse is 20 with respect to a prepulse at  $t = -\tau_0/2 = -15$  fs and 200 with respect to a postpulse at  $t = +\tau_0/2 = 15$  fs. The steep trailing edge of this pulse is indicative of the key role of self-steepening and space-time focusing effects in this regime of pulse compression. The FWHM width of the temporal envelope of  $|A|^2$  on the beam axis at  $z = 0.6$  m is 0.86 fs, which corresponds to 0.3 field cycles [Fig. 5(a)]. Generation of such an extremely short pulse is facilitated by the interference of the spectrally broadened fundamental field

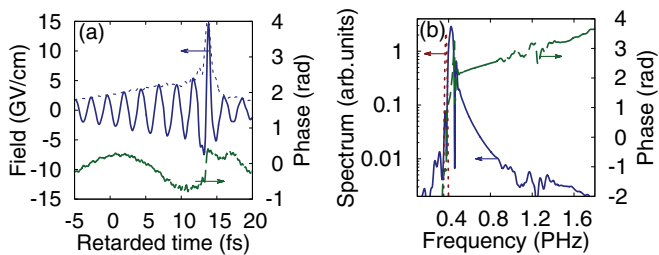


FIG. 5. (Color online) (a) The on-axis electric field (solid blue line) and its envelope (blue dotted line) vs the retarded time and (b) the spectrum of this field waveform at  $z = 0.6$  m for  $E_0 = 6$  J,  $\tau_0 = 30$  fs, and  $P = P_{cr}$ . The green dashed line shows (a) the temporal and (b) the spectral phase of the field. The spectrum of the input pulse is shown in (b) by the dotted red line.

and its third harmonic, which gives rise to fringes, visible in Fig. 3(a). This process enhances the central peak of the field that undergoes the most efficient self-focusing [Fig. 3(a)], giving rise to a solitary peak in the radial profile of the field intensity, which is manifested as a plateau in the dependence of the pulse width on the pinhole diameter in Fig. 4(a). The light intensity achieved in transient field waveforms on the beam axis as a part of this pulse self-compression dynamics is as high as 0.8 EW/cm<sup>2</sup> [ $z = 0.2$  m in Figs. 2(a) and 3(a)], falling in the range of relativistic field intensities.

Generation of relativistic-intensity subcycle field waveforms is quite sensitive to variations in the parameters of the input laser pulse, as well as variations in the gas pressure. Stretching of the input pulse by 3% of its width or a decrease in the input pulse energy by 200 mJ would increase the pulse width at the point of maximum compression inside the filament up to approximately 3.5 fs. As the gas pressure is increased by 20%, the shortest pulse width achieved in the filament is increased to 3 fs.

Even higher field intensities can be generated as a result of filamentation-assisted pulse self-compression dynamics for laser beams with higher input energies. In particular, a laser pulse with  $E_0 = 7$  J and  $\tau_0 = 30$  fs inducing a filament in argon at  $p = 3.1 \times 10^{-5}$  bar generates subcycle field transients with the field intensity as high as 2 EW/cm<sup>2</sup>. The filament length tends to increase with the growth in the input energy in this regime in agreement with the tendency illustrated in Fig. 2(a). Technically, the computer code remains perfectly stable and fully functional in this range of extreme light intensities, while the small-scale features in the spatiotemporal structure of the field can be analyzed using finer adaptive computation steps in space and time. However, since the relativistic physics of light-matter interaction at these cites of extremely high light intensity in filaments is not included in our model and falls beyond the scope of this study, we restrict our analysis here to the regimes where the regions of relativistic light intensity are localized within very small areas, exerting no influence on the overall spatiotemporal dynamics of the laser beam.

We emphasize here that relativistic-intensity subcycle field transients are generated as a part of the considered pulse-compression scenario at a certain propagation distance inside the filament. Filtering this extreme-intensity subcycle field waveform for experiments in the far field is a challenging issue, which may limit the utility of the proposed pulse compression strategy. One possible solution to this problem is to perform relativistic laser-particle interaction experiments (e.g., experiments on particle acceleration) right inside the filament. Our simulations show that by increasing the energy of the input laser pulse up to 7 J, it is possible to generate relativistic-intensity subcycle field transients on a centimeter spatial scale. An alternative solution would be to filter such extreme-intensity subcycle pulses using appropriate pinholes for far-field experiments in the single-shot mode, which is not uncommon for extreme-intensity laser science.

The residual chirp of the pulse at the point of maximum compression [see the contour lines in Fig. 4(c), as well as the profiles of the temporal and spectral phases in Figs. 5(a) and 5(b)] suggests that a further compression of this pulse would be possible with an appropriate dispersion of a medium behind

the filter or a properly designed dispersion-compensating component. The transform-limited pulse width supported by the full spectrum of the pulse at the point of maximum compression is 0.53 fs, which corresponds to 0.2 field cycles.

While argon has been shown to be ideally suited for filamentation-assisted pulse compression to subcycle pulse widths and relativistic field intensities, a similar spatiotemporal dynamics of high-power ultrashort light pulses can be implemented using other gas media. Specifically, neon and krypton, the nearest neighbors of argon in the Periodic Table in the family of rare gases, would be other promising candidates, enabling the expansion of the parameter space for the considered regime of pulse compression. In particular, neon, due to its higher ionization potential, would be suitable for the compression of ultrashort pulses with even higher initial energies (up to 30 J according to our simulations), while krypton would be promising for compression of laser pulses with lower energies (in the range of 0.5–2 J). Obviously, the initial beam diameter and focusing geometry need to be appropriately adjusted for efficient pulse compression in other gas media.

Higher-order nonlinearities, included in our model through the  $n_4$  terms in Eqs. (1) and (2), may play a significant role in pulse self-compression in the regime of extreme light intensities. While positive  $n_4$  values tend to assist filamentation and pulse compression, negative  $n_4$  may stop self-focusing before the optimal conditions for pulse self-compression are

achieved [Fig. 4(d)]. Under these conditions, the optimal gas pressure and initial beam focusing should be redefined with the inclusion of the  $n_4$  effects for the maximum efficiency of pulse self-compression.

## V. CONCLUSION

We have shown that filamentation-assisted spatiotemporal dynamics of ultrashort laser pulses in the regime of extreme light powers can enable self-compression of subpetawatt laser pulses to subcycle pulse widths and relativistic field intensities. Supercomputer simulations presented here demonstrate compression of 6-J, 30-fs laser pulses to 1.3-fs sub-100-TW broadband field waveforms and reveal the generation of relativistic-intensity subfemtosecond field transients as a result of such a pulse evolution scenario, with multiple filamentation avoided due to low gas pressures and the balance between Kerr and ionization nonlinearities steered toward optimal pulse compression due to the depletion of ionization from the outer shell of atoms by a high-power laser field.

## ACKNOWLEDGMENTS

We are grateful to A. A. Voronin for fruitful discussions and numerous insightful comments. This work was partially supported by the Welch Foundation (Grant No. A-1801) and Seventh European Framework Programme (CROSS TRAP 244068 project).

- 
- [1] A. Braun, G. Korn, X. Liu, D. Du, J. Squier, and G. Mourou, *Opt. Lett.* **20**, 73 (1995).
  - [2] L. Bergé, S. Skupin, R. Nuter, J. Kasparian, and J.-P. Wolf, *Rep. Prog. Phys.* **70**, 1633 (2007).
  - [3] A. Couairon and A. Mysyrowicz, *Phys. Rep.* **441**, 47 (2007).
  - [4] M. Rodriguez, R. Bourayou, G. Méjean, J. Kasparian, J. Yu, E. Salmon, A. Scholz, B. Stecklum, J. Eisloffel, U. Laux, A. P. Hatzes, R. Sauerbrey, L. Wöste, and J.-P. Wolf, *Phys. Rev. E* **69**, 036607 (2004).
  - [5] C. D'Amico, A. Houard, M. Franco, B. Prade, A. Mysyrowicz, A. Couairon, and V. Tikhonchuk, *Phys. Rev. Lett.* **98**, 235002 (2007).
  - [6] J. Kasparian, M. Rodriguez, G. Méjean, J. Yu, E. Salmon, H. Wille, R. Bourayou, S. Frey, Y. B. Andre, A. Mysyrowicz, R. Sauerbrey, J.-P. Wolf, and L. Wöste, *Science* **301**, 61 (2003).
  - [7] C. P. Hauri, W. Kornelis, F. W. Helbing, A. Heinrich, A. Couairon, A. Mysyrowicz, J. Biegert, and U. Keller, *Appl. Phys. B* **79**, 673 (2004).
  - [8] A. Mysyrowicz, A. Couairon, and U. Keller, *New J. Phys.* **10**, 025023 (2008).
  - [9] F. Reiter, U. Graf, E. E. Serebryannikov, W. Schweinberger, M. Fiess, M. Schultze, A. M. Azzeer, R. Kienberger, F. Krausz, A. M. Zheltikov, and E. Goulielmakis, *Phys. Rev. Lett.* **105**, 243902 (2010).
  - [10] T. Fuji, T. Suzuki, E. E. Serebryannikov, and A. M. Zheltikov, *Phys. Rev. A* **80**, 063822 (2009).
  - [11] A. A. Voronin, S. Ališauskas, O. D. Mucke, A. Pugžlys, A. Baltuška, and A. M. Zheltikov, *Phys. Rev. A* **84**, 023832 (2011).
  - [12] G. A. Mourou and T. Tajima, *Science* **331**, 41 (2011).
  - [13] V. I. Bespalov and V. I. Talanov, *JETP Lett.* **3**, 307 (1966).
  - [14] V. P. Kandidov, O. G. Kosareva, and S. A. Shlenov, *Quantum Electron.* **27**, 443 (1997).
  - [15] M. J. Weber, *Handbook of Optical Materials* (CRC Press, Boca Raton, 2003).
  - [16] C. Bree, A. Demircan, and G. Steinmeyer, *IEEE J. Quantum Electron.* **46**, 433 (2010).
  - [17] J. E. Rice, *J. Chem. Phys.* **96**, 7580 (1992).
  - [18] H. J. Lehmeier, W. Leupacher, and A. Penzkofer, *Opt. Commun.* **56**, 67 (1985).
  - [19] D. P. Sheldon, *Phys. Rev. A* **45**, 2578 (1990).
  - [20] K. Zeil, S. D. Kraft, S. Bock, M. Bussmann, T. E. Cowan, T. Kluge, J. Metzkes, T. Richter, R. Sauerbrey, and U. Schramm, *New J. Phys.* **12**, 045015 (2010).
  - [21] I. Ahmad, S. A. Trushin, Z. Major, C. Wandt, S. Klingebiel, T.-J. Wang, V. Pervak, A. Popp, M. Siebold, F. Krausz, and S. Karsch, *Appl. Phys. B* **97**, 529 (2009).